

Stable numerical technique to calculate the bending of flexures with extreme aspect ratios

Benjamin Schreyer¹, Lorenz Keck², Jon R. Pratt¹, Stephan Schlamming¹

¹National Institute of Standards and Technology, 100 Bureau Drive, Gaithersburg, MD, USA

² SLAC National Accelerator Lab, 2575 Sand Hill Rd, Menlo Park, CA 94025, USA

E-mail: stephan.schlamminger@nist.gov

Abstract. Flexures in torsion balances and precision mechanisms often exhibit extreme aspect ratios, causing exponential scaling in Euler-Bernoulli bending models. Standard double-precision arithmetic cannot resolve the small initial conditions required for accurate solutions. This paper presents a semi-analytic method combining an efficient 1D bending model with adaptive Runge-Kutta-Fehlberg integration in arbitrary precision that overcomes this limitation. A quantitative criterion for when extended precision becomes necessary is established and an open-source Python implementation is provided, which remains stable even for flexures with extreme aspect ratios.

Keywords: arbitrary precision, compliant mechanism, double-precision, Euler-Bernoulli beam, Runge-Kutta-Fehlberg

16 1. Introduction

17 Precision measurement systems often rely on compliant
 18 mechanisms to provide frictionless, repeatable motion.
 19 In applications ranging from the realization of the
 20 mass unit via Kibble balances [1–5] to gravitational
 21 wave detection [6] and micro-force metrology [7–10],
 22 flexures serve as the critical interface between a known
 23 force and a measurable displacement. The performance
 24 of these instruments is fundamentally limited by the
 25 accuracy with which the elastic behavior of the flexures
 26 can be modeled and subsequently measured.

27 In many high-performance metrological instru-
 28 ments, flexures are designed with extreme aspect ra-
 29 tios. These flexures have very long and thin geometries
 30 to minimize parasitic stiffness or to maximize sensitiv-
 31 ity in a specific degree of freedom. However, this geo-
 32 metric optimization introduces a profound challenge
 33 in measurement science: a “computational gap” where
 34 the mathematical models used to predict instrument
 35 behavior become numerically unstable. This instabil-
 36 ity is not a failure of the underlying physics (Euler-
 37 Bernoulli beam theory) but a failure of the standard
 38 numerical representation (IEEE-754 double precision)
 39 to resolve the exponential scaling of the system’s sen-
 40 sitivity.

41 From the perspective of the Guide to the Ex-
 42 pression of Uncertainty in Measurement (GUM) [11], the
 43 reliability of a measurement result is intrinsically linked
 44 to the integrity of the mathematical model of the mea-
 45 surand. In instruments where a compliant mechanism
 46 translates an electrical or gravitational force into a
 47 measurable displacement, the flexure model constitutes
 48 a significant component of the “Type B” evaluation of
 49 uncertainty. For flexures with extreme aspect ratios,
 50 the numerical instability of standard double-precision
 51 solvers can introduce a computational bias that is eas-
 52 ily mistaken for physical non-linearity or experimental
 53 noise.

54 The motivation for this work arises from the need
 55 to ensure that the contribution of numerical error to
 56 the total combined uncertainty remains negligible. Es-
 57 tablishing a quantitative threshold for numerical failure
 58 is therefore essential for preserving the traceability of
 59 the measurement chain in high-sensitivity applications.
 60 High-sensitivity applications include the realization of
 61 mass standards via Kibble balances or the calibration
 62 of small-force standards. Without such a framework,
 63 the accuracy of the instrument becomes limited not by
 64 physical constraints, but by the digital representation
 65 of the model itself.

66 Accurate calculation of flexure deformation is
 67 a prerequisite for determining the sensitivity and
 68 uncertainty budget of precision balances. The well-

posedness and stability of Euler-Bernoulli systems
 69 have been studied in depth [12, 13]. Semi-numerical
 70 methods bridge the gap between closed-form analytical
 71 solutions and computationally intensive finite element
 72 analysis (FEA). While FEA requires discretizing a
 73 full three-dimensional geometry, the semi-analytical
 74 approach reformulates the bending problem into a
 75 system of coupled ordinary differential equations
 76 (ODEs) along a single dimension. By collapsing the
 77 dimensionality of the task, these methods provide
 78 significant computational efficiency. The following
 79 analysis brings these computational gains to the design
 80 of precision flexures.

81 Standard ODE solvers use fixed-precision arith-
 82 metic and often fail when modeling shear-free beam
 83 bending with an *extreme aspect ratio*. In these cases,
 84 the internal bending moment can span many orders
 85 of magnitude, exceeding the dynamic range of the
 86 IEEE 754 double-precision format. To overcome this
 87 limitation, a Runge-Kutta-Fehlberg integrator with
 88 arbitrary-precision floating-point arithmetic is imple-
 89 mented. This enables accurate modeling of flexures
 90 that lie beyond the capability of ODE solvers provided
 91 by common scientific programming languages. A for-
 92 mal criterion for these cases is derived in Sec. 2.3, along
 93 with guidance on the precision required for a given ge-
 94 ometry.

1.1. The Single Flexure

A single flexure under torque and transverse force
 97 represents a fundamental system. However even this
 98 basic configuration challenges numerical methods due
 99 to precision loss at extreme aspect ratios. Fig. 1
 100 illustrates a flexure supporting a weight $F_w = mg$
 101 while being subjected to a transverse force F_d at its
 102 free end ($s = L$). The variable s measures distance
 103 along the neutral axis from the clamp $s = 0$ to the
 104 tip $s = L$. The angle $\theta(s)$ is measured relative to
 105 the vertical, with the clamped boundary condition
 106 $\theta(0) = 0$. The internal bending moment is denoted
 107 by $M(s)$. The deformation of the flexure is governed
 108 by coupled differential equations:

$$\frac{dM}{ds} = F_w(s) \sin \theta(s) + F_d(s) \cos \theta(s) \quad (1a)$$

$$\frac{d\theta}{ds} = \frac{M(s)}{E(s)I(s)}, \quad (1b)$$

where $E(s)$ denotes the elastic modulus and $I(s)$ the
 110 second moment of area about the neutral axis. For
 111 uniform beams, $E(s)$, $F_w(s)$, and $F_d(s)$ are treated as
 112 constants.

The flexural stiffness is determined by the specific
 113 cross-sectional geometry. For circular sections of radius

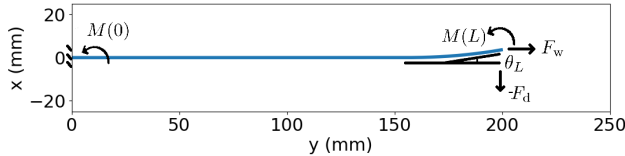


Figure 1: Schematic of a 200 mm flexure clamped at $s = 0$. In this coordinate system, gravity acts along the $+y$ direction. An applied tip moment produces a final angle of $\theta_L = 10^\circ$. The arc-length coordinate s follows the neutral axis.

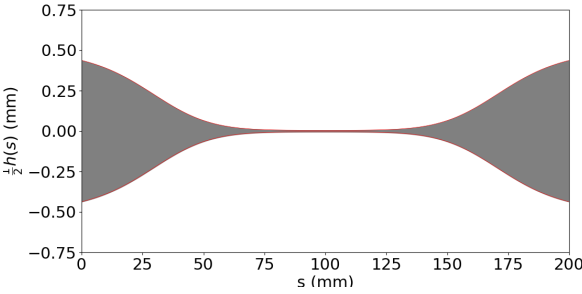


Figure 2: Profile of a planar flexure where the thickness reduces by a factor of 100 at the waist. Simulation parameters are $E = 1.31 \times 10^5$ MPa, $F_w = 1$ N, $b = 0.1$ mm. This extreme geometry causes standard double-precision (float64) shooting algorithms to fail.

¹¹⁶ $r(s)$ and rectangular sections of fixed width b and
¹¹⁷ varying thickness $h(s)$, the second moments of area
¹¹⁸ are:

$$I_o(s) = \frac{\pi}{4} r^4(s) \text{ and} \quad (2a)$$

$$I_{\square}(s) = \frac{1}{12} b h^3(s). \quad (2b)$$

¹¹⁹ These parameters may vary with s , see Fig. 2,
¹²⁰ a dependency that precludes closed-form analytical
¹²¹ solutions for the deflection profile.

¹²² The flexure bending is modeled as a two-point
¹²³ boundary-value problem and solved using a shooting
¹²⁴ method [14, 15]. The unknown initial moment $M(0)$ is
¹²⁵ iteratively adjusted until the terminal angle $\theta(s = L)$
¹²⁶ matches the target $\hat{\theta}$. Standard IEEE-754 double
¹²⁷ precision can only represent normal numbers down to
¹²⁸ $\approx 2.2 \times 10^{-308}$. However, the geometry shown in Fig. 1
¹²⁹ requires moments spanning $M(0)/M(L) \sim 10^{-596}$.
¹³⁰ This dynamic range causes standard double-precision
¹³¹ (float64) solvers to underflow. Consequently, higher-
¹³² precision arithmetic beyond double precision (float64)
¹³³ is required to obtain a convergent solution.

¹³⁴ A uniform flexure with $F_d = 0$ illustrates the
¹³⁵ numerical challenge. The analytical solution given by

Speake [16] is

$$M(0) = 2M(L)e^{-\alpha L} \text{ with } \alpha^2 = \frac{F_w}{EI}. \quad (3)$$

The ratio $M(0)/M(L)$ scales exponentially with decay length α^{-1} . For sufficiently small I or large L , this ratio exceeds the dynamic range of IEEE-754 double precision (float64), causing standard shooting methods to fail.

Analytical solutions are limited to uniform flexures, whereas practical designs often utilize non-uniform geometries. Numerical strategies for the resulting governing equations include relaxation [15, 17] and shooting methods. While shooting techniques are effective for moderate aspect ratios [4, 18], the following analysis extends the method to the extreme aspect ratio regime.

1.2. The Shooting Method

The coupled bending equations, Eq. (1), are numerically integrated to determine the deflection profile. A shooting method [14, 15] enforces the boundary conditions, specifically the clamping angle and the target end angle $\hat{\theta}$. This technique transforms the boundary-value problem into an initial-value problem where the unknown initial moment $p = M(0)$ is iteratively adjusted. The iteration minimizes the residual function:

$$G(p) = \theta_L(p) - \hat{\theta}, \quad (4)$$

where $\theta_L(p)$ is the integrated end angle for a given trial p . For flexures with extreme aspect ratios, standard double-precision (float64) arithmetic fails. The required initial moment p becomes so small that it underflows the floating-point representation. Consequently, the root-finder cannot locate the specific $M(0)$ required to satisfy the condition $\theta_L(p) = \hat{\theta}$. The flexure shown in Fig. 2 is a geometry where such failure occurs.

1.3. Floating-point Representation

The inherent limitations of fixed-precision arithmetic are well established. Restricted exponent ranges hinder calculations involving Legendre polynomials [19, 20], while insufficient precision causes numerical orbits to lose periodicity [21]. Standard precision also fails to capture the behavior of chaotic systems, such as the Lorenz attractor [22], leading to spurious solutions that are purely numerical artifacts [23]. While dynamic analysis can diagnose these errors [24, 25], the fundamental constraint remains the finite representation of the number system.

A floating-point number N comprises three components: a sign bit (\pm), an unsigned integer δ (bit

width d) encoding the mantissa (or significand), and a signed integer λ (bit width l) encoding the exponent. For normalized numbers, implicit leading bit defines the value as:

$$N = \pm\left(1 + \frac{\delta}{2^d}\right) \cdot 2^\lambda. \quad (5)$$

The IEEE standard [26] allocated 64 bits for double precision binary (float64): 1 sign bit, $l = 11$ exponent bits, and $d = 52$ mantissa bits. The exponent employs a bias of $1023 = 2^{(l-1)} - 1$, yielding an effective normal range of $-2^{(l-1)} + 2 = -1022 \leq \lambda \leq 2^{(l-1)} - 1 = 1023$. This corresponds to a representable magnitude range from $\approx 2.2 \times 10^{-308}$ to $\approx 1.8 \times 10^{308}$.

Subnormal numbers extend the minimum representable magnitude to $\approx 5 \times 10^{-324}$. These values are encoded with a zero in the exponent field, corresponding to a fixed exponent $\lambda = -1022$ and no implicit leading bit. The value is given by

$$N = \pm\frac{\delta}{2^d} \cdot 2^{-1022}. \quad (6)$$

While this mechanism allows for gradual underflow, it sacrifices significant digits, rendering subnormals unsuitable for high-precision integration. Consequently, the following analysis is restricted to the dynamic range defined by normalized numbers.

The *effective dynamic range* of a format with l exponent bits is defined as the ratio of unity to the smallest positive normal number, approximately 2^{l-1} . This definition excludes the positive exponent range, a restriction justified by the physics of the bending problem. Since the maximum deflection $\theta(L)$ is of order unity, the solution for $s < L$, $\theta(s)$ occupies the negative exponent range. Supporting this specific range allows the system to be solved directly without variable rescaling (see Section 1.4).

Quadruple precision (float128) with $l = 15$ offers a dynamic range of $\approx 10^{4932}$. This magnitude is sufficient for the extreme geometries analyzed in this work. To implement this capability, the Python library mpmath [27] is utilized. This library supports arbitrary-precision floating-point arithmetic, ensuring that the dynamic range encompasses the physical requirements detailed in Section 2.3.

1.4. Why Rescaling Cannot Replace Extended Precision

Variable rescaling is a standard technique for mitigating numerical errors. For instance, the moment $M(s)$ can be normalized by a reference moment M_n . However, as demonstrated in Eq. (3), the ratio $M(L)/M(0)$ spans hundreds of orders of magnitude. A global scaling factor shifts the absolute magnitudes but preserves

this ratio. Therefore, if the ratio exceeds the intrinsic dynamic range of the floating-point format, global rescaling cannot prevent underflow or overflow.

Adaptive piecewise scaling $\gamma(s)$ could theoretically accommodate the range but introduces significant complexity regarding continuity and boundary conditions. Furthermore rescaling the angle is impeded by the nonlinearity of the trigonometric functions. For example, a Taylor approximation, of $\theta(s)$ rescaled as $\theta(s) = \gamma\theta_n(s)$, yields

$$\cos \theta(s) = \cos(\gamma\theta_n(s)) \approx 1 - \frac{1}{2}\gamma^2\theta_n(s)^2. \quad (7)$$

Rescaling cannot resolve the dynamic range deficit, leaving extended floating-point width the most practical solution.

2. Analytical Solutions

Analytical solutions illustrate the origin of the numerical instability encountered in thin flexures. These solutions reveal the exponential growth of moments and angles, rendering standard double-precision arithmetic insufficient.

2.1. Large Exponents in Bending

The moment at the clamp $M(0)$ is exceptionally small, yet it must remain finite to achieve the target deflection. When $F_d = 0$, a zero initial moment results in a trivial straight-beam solution. A non-zero moment is required to break the axial symmetry and initiate bending. The solution in Fig. 1 was determined with a very small initial value $M(0)$.

Using the parameters listed in Table 1, the deflection profile can be obtained by shooting from an exceptionally small initial moment $M(0)$. Specifically, achieving a target deflection of 1 rad requires $M(0) \approx 1 \times 10^{-330}$ Nm. This magnitude lies beneath the representable range of double precision (float64). The exponential growth of the bending moment and fiber angle across the flexure length exacerbates the limitations of finite-precision arithmetic, rendering the solution unreachable without extended exponent range.

2.2. Small-angle Solutions

Solutions for beam deformation involving hyperbolic trigonometric functions are well established in the literature [16, 28]. Revisiting these solutions highlights the exponential growth that drives numerical instability. Because solutions satisfying the clamping condition $\theta(0) = 0$ track the small-angle limit near the fixed end, the numerical constraints identified in the linear regime persist in large-deflection problems.

Table 1: Parameters of a circular cross section flexure used in [6], assuming $F_d = 0$. Input properties are listed above the horizontal rule, with derived parameters shown below.

| Par. | Eq. | Value |
|------------------------|-------------------|---------------------------------------|
| E | | 7.3×10^{10} N/m ² |
| L | | 6.00×10^{-1} m |
| r | | 2.00×10^{-4} m |
| F_w | mg | 1.47×10^2 N |
| F_d | | 0 N |
| I | $\pi r^4/4$ | 1.26×10^{-15} m ⁴ |
| α | $\sqrt{F_w/(EI)}$ | 1.27×10^3 m ⁻¹ |
| αL | | 7.60×10^2 |
| $[2^{l-1} \ln 2]_{50}$ | for $l = 11$ | 7×10^2 |
| $e^{\alpha L}$ | | 1.16×10^{330} |
| σ_w | $F_w/(r^2\pi)$ | 1.176×10^9 N/m ² |
| $\sqrt{E/\sigma_w}$ | | 7.90 |
| L/r | | 3.00×10^3 |

277 A uniform flexure ($I(s) = I_0$) where $\alpha L \gg 1$
278 characterizes the exponential behavior.

279 The analytical solutions from Speake [16] are
280 mapped to the (s, θ) domain, where the approximation
281 $x \approx s$ is valid for small angles. In the regime $\alpha L \gg$
282 1, the hyperbolic functions simplify to $\sinh(\alpha L) \approx$
283 $\cosh(\alpha L) \approx \frac{1}{2}e^{\alpha L}$. Applying these to Eqs. (1) and (2)
284 of [16] yields

$$M(L) \approx \frac{1}{2} \left(M(0) - \frac{F_d}{\alpha} \right) e^{\alpha L}. \quad (8)$$

285 The terminal angle $\theta(L)$ is determined via the
286 compliance matrix [16]

$$\theta(L) \approx \frac{F_d}{F_w} (1 - 2e^{-\alpha L}) + \frac{\alpha M(L)}{F_w}. \quad (9)$$

287 Substituting Eq. (8) into Eq. (9) relates the terminal
288 angle directly to the initial moment,

$$\theta(L) \approx \frac{F_d}{F_w} \left(1 - 2e^{-\alpha L} - \frac{e^{\alpha L}}{2} \right) + \frac{M(0)}{2F_w} e^{\alpha L} \quad (10)$$

289 Removing small terms from the parenthetical sum
290 yields the approximation

$$\theta(L) \approx \frac{1}{2F_w} \left(\alpha M(0) - F_d \right) e^{\alpha L}. \quad (11)$$

291 This expression highlights the extreme sensitivity of
292 $\theta(L)$ to the initial moment $M(0)$ and the transverse

load F_d . In the regime of extreme aspect ratios, the $e^{\alpha L}$ term becomes so large that $M(0)$ must be infinitesimally small to yield a physical $\theta(L)$, precipitating the floating-point underflow described in Section 1.3. The agreement between this exponential approximation and the numerical results is illustrated in Fig. 3.

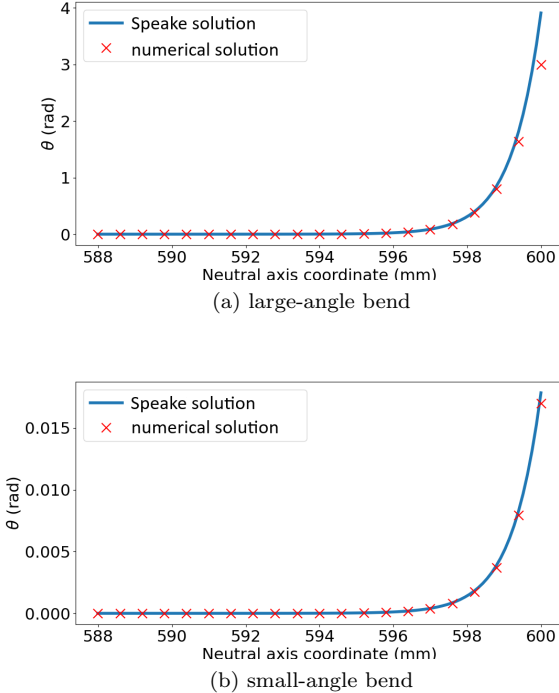


Figure 3: Bending of a loaded flexure under torque, using the parameters in Table 1, shown over the final 12 mm of the flexure. Panel (a) shows a large deflection, while panel (b) shows a small deflection. In panel (a), the breakdown of the small-angle approximation is evident as the small-angle solution deviates from the numerical result.

2.3. When Is a Flexure Considered Extreme Aspect Ratio?

The analytical solution above allows formal definition of the conditions under which a flexure is considered to have an extreme aspect ratio, relative to the available floating-point exponent range.

Consider a flexure with constant circular-cross section loaded by a force F_w , resulting in a stress

$$\sigma_w = \frac{F_w}{\pi r^2}. \quad (12)$$

According to Eq. (11), the dynamic range required for the computation scales as $\exp(\alpha L)$ since parameters $F_d, \alpha, M(0)$ must be represented numerically along

with $\theta(L)$ which is exponentially larger. A flexure is defined as having an extreme aspect ratio if this required dynamic range exceeds the representable range of a binary floating-point number with exponent bit width l , i.e.,

$$e^{\alpha L} > 2^{2^{l-1}} \rightarrow \alpha L > 2^{l-1} \ln 2. \quad (13)$$

This threshold reflects the maximum dynamic range permitted by the floating-point exponent, see Section 1.3.

For a circular cross-section, the stability criterion implies:

$$\alpha L = L \sqrt{\frac{4F_w}{E\pi r^4}} > 2^{l-1} \ln 2 \quad (14)$$

Combining Eq. (12) and Eq. (14) yields a compact criterion for when a flexure exceeds the capacity of a given floating-point format:

$$\frac{L}{r} > \underbrace{\frac{\ln 2}{4}}_{0.17} \sqrt{\frac{E}{\sigma_w}} 2^l. \quad (15)$$

To generalize this condition for non-uniform geometries, the stability threshold is defined as the nearest multiple of a safety margin N_{margin} denoted by $\lfloor \cdots \rfloor_{N_{\text{margin}}}$

$$\alpha L < \underbrace{\lfloor 2^{l-1} \ln 2 \rfloor}_{\beta} N_{\text{margin}}. \quad (16)$$

For example with $N_{\text{margin}} = 50$, $l = 11$, one obtains $2^{l-1} \ln 2 = 709.8$ and, hence, $\beta = \lfloor 2^{l-1} \ln 2 \rfloor_{50} = 700$.

For a flexure with variable cross section, the condition must hold for the maximum value α^* :

$$\alpha^* L = \max_{s \in [0, L]} \left(\sqrt{\frac{F_w}{EI(s)}} \right) L < \beta. \quad (17)$$

This approach effectively compares the actual flexure to a hypothetical “worst-case” uniform beam with constant α^* . Since this hypothetical beam is more compliant than the actual geometry, it provides a conservative upper bound on the required numerical dynamic range. While more refined estimates could be derived using the WKB method, this simpler bound is sufficient given the coarse discretization of available floating-point standards.

Table 2 summarizes the floating-point precision required to satisfy the stability condition for various bit-widths l . The listed β values assume a safety margin $N_{\text{margin}} = 50$, ensuring the threshold remains non-zero for all standard formats. Applying this limit to flexure in Table 1, yields a product $\alpha L = 760$ which exceeds the double precision threshold $\beta_{\text{double}} = 700$. Consequently, IEEE-754 double precision is inadequate for this case, necessitating the use of quadruple precision ($\beta_{\text{quadruple}} = 11350$).

2.4. Numerical Conditioning of Large-Angle Bending Solutions

In the small-angle regime, the linear nature of the system ensures that the terminal angle $\theta(L)$ relates linearly to the initial conditions. This linear mapping provides favorable numerical conditioning, as the precision of the initial parameters is preserved at the boundary. At large deflections, however, the trigonometric terms depart from their zero-centered linearizations and begin to saturate.

Recall that the exponential growth responsible for floating-point exponent limitations arises from the linear behavior near $\theta = 0$. To determine a lower bound on sensitivity in the nonlinear regime, we assume the trigonometric variations become small and can be approximated as constants. This yields:

$$\frac{dM}{ds} \sim F_w, \quad (18a)$$

$$\frac{d\theta}{ds} = \frac{M(s)}{EI(s)}. \quad (18b)$$

For a uniform cross section, integrating these relations for the remaining growth after saturation ($s > L_s$, where the subscript s denotes the saturation point) gives:

$$\theta(L) - \theta(L_s) \sim \frac{L - L_s}{EI} \left(M(L_s) + \frac{F_w}{2} (L - L_s) \right) \quad (19)$$

At L_s , θ reaches unity and the exponential growth concludes:

$$\theta(L_s) \approx \frac{1}{2F_w} (\alpha M(0) - F_d) e^{\alpha L_s} \approx 1 \quad (20)$$

Solving for L_s yields

$$-L_s \approx \ln \left(\frac{\alpha M(0) - F_d}{2F_w} \right) \frac{1}{\alpha}. \quad (21)$$

Substituting L_s and $M(L_s)$ into Eq. (19) yields

$$\theta(L) \sim 1 + X + \frac{1}{2} X^2, \quad (22)$$

with

$$X = \alpha L + \ln \left(\frac{\alpha M(0) - F_d}{2F_w} \right). \quad (23)$$

If saturation is immediate or equivalently F_d dominates the variation of M Eq. (19) has $F_w \rightarrow F_d$ and the result is a bounding linear relation between $M(0)$ and the end angle. This approximation demonstrates that the system exhibits, at worst, logarithmic sensitivity when modulating the initial conditions to achieve a nonlinear terminal angle. Thus, the exponent bits of the floating-point representation play the decisive role in shooting for large-angle solutions, as these bits represent the logarithm of the initial condition. For non-uniform geometries, a conservative upper bound can be maintained by considering the most compliant sections of the flexure.

Table 2: IEEE 754 precision requirements for the bending solver. The condition that $\alpha^* L < \beta$ ensures that the selected format provides sufficient dynamic range for accurate computation. The column labeled ϵ lists the smallest positive normalized number representable in each format.

| name | total bits | exp. bits, l | ϵ | β |
|-----------|---------------|-------------------|--------------------------|------------------------|
| | | | | $[2^{l-1} \ln 2]_{50}$ |
| single | 32 | 8 | 1×10^{-38} | 50 |
| double | 64 | 11 | 2×10^{-308} | 700 |
| quadruple | 128 | 15 | 3.3×10^{-4932} | 11 350 |
| octuple | 256 | 19 | 1.5×10^{-78913} | 181 700 |

3. Practical Tips for the Shooting Method

To compute a bending solution for a desired end angle $\hat{\theta}$, a shooting method is employed, designating the initial bending moment $M(0)$ as the shooting parameter p . The objective is to find a value p for which the numerical solution satisfies $\theta(L) = \hat{\theta}$. A two-stage approach is implemented, following established numerical strategies [14, 15]. The first stage initializes the calculation with p^* , the smallest magnitude normal value in the floating-point format being used. Integrating the ODEs with this p^* yields a corresponding trial bending angle $\theta^* = \theta_L(p^*)$. Exploiting the linearity of the system at these infinitesimal magnitudes, the initial moment required to reach the target angle $\hat{\theta}$ can be estimated by scaling [14]:

If the desired angle is small, $\hat{\theta} < \theta_{\text{small}}$ with $\theta_{\text{small}} = 0.1 \text{ rad}$, the parameter is set as

$$p^\dagger = \frac{\hat{\theta}}{\theta^*} p^*. \quad (24)$$

Otherwise, to ensure convergence despite nonlinearity of trigonometric functions at large angles, θ_{small} is instead the target and the parameter set as

$$p^\dagger = \frac{\theta_{\text{small}}}{\theta^*} p^*. \quad (25)$$

This yields an initial condition that produces an end angle of the correct order of magnitude.

In the second stage, the linear estimate is refined using a nonlinear root-finding algorithm. Specifically, the Anderson-Björck method [29] is applied to solve $G(p) = \theta_L(p) - \hat{\theta} = 0$, with $p \in [p^\dagger/64, 64p^\dagger]$ around the linearized guess as the search domain.

This two-step process was successfully tested for a variety of flexure geometries. The initial scaling phase effectively localizes the search range, ensuring that the second stage converges reliably to the required, often infinitesimal, value of $M(0)$. The algorithm is fully compatible with the arbitrary-precision arithmetic provided by mpmath [27], allowing for seamless scaling

of the dynamic range as required by the flexure aspect ratio. The implementation logic is summarized in the pseudo-code below.

Algorithm 1 Two step algorithm to find an initial condition p , e.g. $M(0)$, that gives an end angle $\hat{\theta}$. Subroutine APRKF45(p) numerically integrates the bending differential equation for initial condition p in arbitrary precision and returns the end angle $\theta_L(p)$.

```

1: procedure BEND TO  $\hat{\theta}$ , VARY  $p$ 
2:    $\theta_{\text{small}} \leftarrow 0.1 \text{rad}$ 
3:    $p^* \leftarrow \text{smallest magnitude floating-point value}$ 
4:    $\theta^* \leftarrow \text{APRKF45}(p^*)$ 
5:   if  $\hat{\theta} < \theta_{\text{small}}$  then
6:      $p^\dagger \leftarrow \frac{\hat{\theta}}{\theta^*} p^*$ 
7:   else
8:      $p^\dagger \leftarrow \frac{\theta_{\text{small}}}{\theta^*} p^*$ 
9:    $S \leftarrow [\frac{1}{64}p^\dagger, 64p^\dagger]$ 
10:  return root(APRKF45( $p$ ) -  $\hat{\theta}$ ) for  $p \in S$ 

```

The conditioning of the auxiliary function $G(p)$ can be characterized for the large-angle regime following the sensitivity analysis in Section 2.4. Based on the approximation in Eq. (22), and assuming that $M(0)$ and F_d depend linearly on the shooting parameter p , the magnitude of the derivative satisfies:

$$|G'(p)| > \left| \frac{1}{p} \right|. \quad (26)$$

Hence, an error ϵ in the evaluation of $G(p)$ will result in a relative error of the root of order ϵ or less.

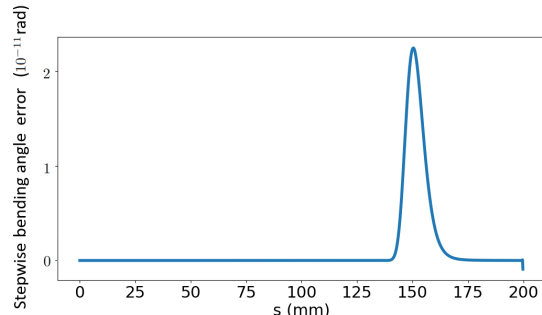
3.1. Computational Performance and Numerical Error

The solver utilizes an arbitrary-precision Runge-Kutta-Fehlberg 45 (APRKF45) scheme, which employs fourth- and fifth-order coefficients to ensure bounded numerical errors. For non-uniform geometries, the

441 varying moment of inertia $I(s)$ is sampled and recon-
 442 structed using cubic splines. To optimize performance,
 443 an APRKF89 variant utilizing eighth- and ninth-order
 444 coefficients [30, 31] was also implemented. This ad-
 445 dition significantly accelerates calculations for many
 446 cross sections.

447 Stepwise error estimates are provided by embed-
 448 ded methods. Errors for the chosen flexure parameters
 449 were much smaller than a practical angular tolerance
 450 with APRKF45. The stepwise error is shown in Fig. 4
 451 for an analytically intractable bending problem. In
 452 Fig. 4 the estimated error is associated with solving
 453 $F_d = 0$ bending with 1000 uniformly spaced integrator
 454 steps for a ribbon as in Fig. 2 with bending geometry
 455 shown in Fig. 1. These parameters can only be solved
 456 by shooting from the clamped end if the computer sys-
 457 tem can represent $M(0) \sim 10^{-596} \text{ N m}$.

458 Numerical stability was verified by decreasing the
 459 step size and confirming convergence of the bending
 460 geometry. Test bending problems were solved in
 461 tens of seconds using our Python implementation.
 462 This runtime could be reduced to milliseconds
 463 by enabling Runge-Kutta-Fehlberg adaptive step-
 464 sizing and re-implementing the solver in a compiled
 465 language such as C++ or Fortran. The Python
 466 implementation used in this work is available at:
 467 <https://github.com/usnistgov/BeamBending>.



468 Figure 4: Estimated local truncation error $\Delta\theta$ across
 469 1000 integrator steps for the profile $\theta(s)$, calculated
 470 using the embedded APRKF45 algorithm [30] for the
 471 non-uniform flexure geometry in Fig. 2. These internal
 472 error estimates provide a vital validation metric in
 473 the absence of a closed-form analytical solution for
 474 the variable cross-section case. As a baseline for
 475 reliability, the truncation errors remain several orders
 476 of magnitude below the target angular values.

477 The numerical solver is compared against the
 478 closed-form hyperbolic sine solution for a uniform
 479 beam with $F_d = 0$. A circular flexure with parameters
 480 listed in Table 1 serves as a test case. This
 481 specific geometry requires a floating-point exponent
 482 range beyond double precision. Fig. 3 displays

483 results for target angles of 3 rad and 0.017 rad. The
 484 larger deflection illustrates the expected breakdown
 485 of the small-angle approximation, while in the
 486 small-deflection regime, the numerical and analytical
 487 solutions are in excellent agreement.

4. Conclusions

488 This work establishes a robust and efficient numerical
 489 framework for simulating compliant mechanisms with
 490 extreme-aspect-ratio flexures. We identify the specific
 491 regimes where standard double precision (float64)
 492 is fundamentally insufficient due to the exponential
 493 sensitivity of the initial shooting parameter to the
 494 terminal boundary conditions. By formalizing the
 495 relationship between flexure geometry and numerical
 496 dynamic range, we provide a definitive criterion for the
 497 transition to extended-precision arithmetic.

498 The use of arbitrary-precision Runge-Kutta-
 499 Fehlberg integrators ensures stable and accurate
 500 modeling in regimes where conventional solvers fail.
 501 Our open-source Python implementation facilitates the
 502 fast, reliable design of non-uniform flexures across a
 503 wide range of geometries, providing a critical utility for
 504 the design of high-precision instruments and advanced
 505 compliant mechanisms.

Acknowledgments

506 We thank our NIST colleagues Jack Manley and John
 507 Lawall for their valuable feedback on the manuscript.

References

- [1] Robinson I A and Schlamming S 2016 *Metrologia* **53** A20
- [2] Keck L 2025 *Flexure-based mechanism for a Kibble Balance* Ph.D. thesis Ilmenau dissertation, Technische Universität Ilmenau, 2024 URL https://www.db-thueringen.de/receive/dbt_mods_00063554
- [3] Keck L, Shaw G, Theska R and Schlamming S 2021 *IEEE Transactions on Instrumentation and Measurement* **70** 1–9
- [4] Keck L, Schlamming S, Theska R, Seifert F and Haddad D 2024 *Metrologia* **61** 045006 URL <https://dx.doi.org/10.1088/1681-7575/ad57cb>
- [5] Green O R, Bao Y, Lawall J R, Gorman J J and Barker D S 2024 *arXiv preprint arXiv:2409.00256* 15 (Preprint 2409.00256) URL <https://doi.org/10.48550/arXiv.2409.00256>
- [6] Aston S M, Barton M A, Bell A S, Beveridge N, Bland B, Brummitt A J, Cagnoli G, Cantley C A, Carbone L, Cumming A V, Cunningham L, Cutler R M, Greenhalgh R J S, Hammond G D, Haughian K, Hayler T M, Heptonstall A, Heefner J, Hoyland D, Hough J, Jones R, Kissel J S, Kumar R, Lockerbie N A, Lodhia D, Martin I W, Murray P G, O'Dell J, Plissi M V, Reid S, Romie J, Robertson N A, Rowan S, Shapiro B, Speake C C, Strain K A, Tokmakov K V, Torrie C, van Veggel A A, Vecchio A and Wilmut I 2012 *Class. Quantum Gravity* **29** 235004

- [7] Arumugam K and Shaw G 2023 *Measurement Science and Technology* **34** 081002 URL <https://doi.org/10.1088/1361-6501/acd134>
- [8] Arumugam K, Cripe J, Schulze S, Schlamming S and Shaw G 2026 *Measurement Science and Technology* **37** 035001 URL <https://doi.org/10.1088/1361-6501/ae2af>
- [9] Shaw G A, Stirling J, Kramar J A, Moses A, Abbott P, Steiner R, Koffman A, Pratt J R and Kubarych Z J 2016 *Metrologia* **53** A86 URL <https://doi.org/10.1088/0026-1394/53/5/A86>
- [10] Pratt J R, Smith D T, Nayfeh P R and Newell D B 2005 *Journal of Research of the National Institute of Standards and Technology* **110** 667
- [11] Joint Committee for Guides in Metrology (JCGM) 2008 *Evaluation of measurement data – Guide to the expression of uncertainty in measurement (GUM)* 1st ed (BIPM) jCGM 100:2008 URL <https://www.bipm.org/en/publications/guides/gum.html>
- [12] Deng P, Zheng J and Zhu G 2024 *Commun. Anal. Mech.* **16** 193–216
- [13] Edalatzadeh M S and Morris K A 2019 *IEEE Control Syst. Lett.* **3** 162–167
- [14] Stoer J and Bulirsch R 2002 *Introduction to numerical analysis* 3rd ed ISBN 978-1-4419-3006-4
- [15] Press W H, Teukolsky S A, Vetterling W T and Flannery B P 2007 *Numerical Recipes: The Art of Scientific Computing* 3rd ed (Cambridge University Press) ISBN 9780521880688
- [16] Speake C C 2018 *Metrologia* **55** 114 URL <https://dx.doi.org/10.1088/1681-7575/aaa112>
- [17] Perrone N and Kao R 1971 *J. Appl. Math. Mech.* **38** 371–376 ISSN 0021-8936 (*Preprint* https://asmedigitalcollection.asme.org/appliedmechanics/article-pdf/38/2/371/5451411/371_1.pdf) URL <https://doi.org/10.1115/1.3408785>
- [18] Henning S and Zentner L 2021 *Mech. Mach. Theory* **164** 104397 ISSN 0094-114X URL <https://www.sciencedirect.com/science/article/pii/S0094114X21001555>
- [19] Smith J M, J O F W and Lozier D W 1981 *ACM Trans. Math. Softw.* **7** 93–105 URL <https://api.semanticscholar.org/CorpusID:15787346>
- [20] Fukushima T 2012 *J. Geod.* **86** 271–285 ISSN 1432-1394 URL <https://doi.org/10.1007/s00190-011-0519-2>
- [21] Abad A, Barrio R and Dena A 2011 *Phys. Rev. E* **84**(1) 016701 URL <https://link.aps.org/doi/10.1103/PhysRevE.84.016701>
- [22] Wang P, Huang G and Wang Z 2006 *Adv. Atmos. Sci.* **23** 758–766
- [23] Allen E, Burns J, Gilliam D, Hill J and Shubov V 2002 *Math. Comput. Model.* **35** 1165–1195 ISSN 0895-7177 URL <https://www.sciencedirect.com/science/article/pii/S089571770200078X>
- [24] Benz F, Hildebrandt A and Hack S 2012 *SIGPLAN Not.* **47** 453–462 ISSN 0362-1340
- [25] Barr E T, Vo T, Le V and Su Z 2013 *SIGPLAN Not.* **48** ISSN 0362-1340
- [26] 2019 *IEEE Std 754-2019 (Revision of IEEE 754-2008)* 1–84
- [27] Johansson F *et al.* 2023 mpmath: a Python library for arbitrary-precision floating-point arithmetic accessed: 2025-05-28 URL <https://mpmath.org/>
- [28] Quinn T J, Speake C C and Davis R S 1986 *Metrologia* **23** 87 URL <https://dx.doi.org/10.1088/0026-1394/23/2/002>
- [29] Anderson N and Björck A 1973 *BIT Numer. Math.* **13** 253–264
- [30] Fehlberg E 1964 *Zamm-zeitschrift Fur Angewandte Mathematik Und Mechanik* **44** URL <https://api.semanticscholar.org/CorpusID:203026934>